ADVANCED ELECTRONIC MATERIALS
www.advelectronicmat.de

# π-Conjugated Organosilica Semiconductors: Toward Robust Organic Electronics

*Gilles H. Roche, Damien Thuau, Pierre Valvin, Simon Clevers, Thomas Tjoutis, Sylvain Chambon, David Flot, Yves H. Geerts, Joël J. E. Moreau, Guillaume Wantz,* and Olivier J. Dautel**

**The use of novel organosilica materials embedding π-conjugated moieties as semiconductor into field-effect transistors is demonstrated. The chosen π-conjugated core is a [1]benzothieno[3,2-b][1]benzothiophene that is modified with hydrolyzable and crosslinkable triethoxysilyl moieties. After polycondensation, this compound forms a hybrid material composed of charge transport pathways as well as insulating sublayers made of silicon oxide ($SiO_x$). The hybrid material behaves as a semiconductor and is subsequently integrated as active layer into field-effect transistors. These precursors show J-type aggregation that evolves toward H-type aggregates during the sol–gel process, which improve charge transport. Taking advantage of the sol–gel chemistry involved here, hybrid field-effect transistors that are fully crosslinked with covalent bonds are built. Molecules are crosslinked to each other, covalently bonded to the silicon oxide dielectric, and also covalently bonded to the gold electrodes, thanks to the use of an appropriate additional interfacial monolayer. This is the first report of fully covalent transistors. Those devices with modest mobilities show impressive resilience against polar, aliphatic, and aromatics solvents even under sonication. This study opens the route toward a new class of hybrid materials to create highly robust electronic applications.**

## 1. Introduction

Materials derived from organic π-conjugated molecules and polymers have generated extensive academic and industrial interest as semiconductors in electronic and photonic applications ranging from organic light emitting diodes (OLEDs),[1,2] photovoltaic solar cells[3] to organic field-effect transistors (OFETs).[4] To date, OLED displays have delivered the most significant large scale commercial impact.[5] These devices share a common trait: in all instances, their performance critically depends on charge carrier motion (electrons and/or holes) within the π-conjugated material. As a result, the performance of organic electronic devices is mainly determined by the chemical structure, the purity, the supramolecular organization and/or the morphology of the π-conjugated material. Molecular engineering combined with supramolecular chemistry form a set of interesting alternatives for the bottom-up design of organic semiconducting materials.[5] Controlled aggregation of π-conjugated systems offers interesting electronic and photonic functional materials that are different from their monomeric state. The self-association of chromophores in the solid or at the solid–liquid interface is a frequently encountered phenomenon in dye and pigment chemistry owing to strong intermolecular van der Waals-like attractive forces between molecules. The aggregates in the solid state exhibit distinct changes in the absorption band as compared to the monomeric species.[6]

G. H. Roche, T. Tjoutis, Prof. J. J. E. Moreau, Dr. O. J. Dautel
Institut Charles Gerhardt Montpellier
UMR CNRS 5253
Architectures Moléculaires et Matériaux Nanostructurés
Ecole Nationale Supérieure de Chimie de Montpellier
8 rue de l'école normale, Montpellier Cedex 5, 34296, France
E-mail: olivier.dautel@enscm.fr

Dr. D. Thuau, Dr. S. Chambon, Dr. G. Wantz
Bordeaux Institute of Technology (Bordeaux INP/ENSCBP)
IMS CNRS UMR 5218
University of Bordeaux
16 Avenue Pey Berland, Pessac F-33607, France
E-mail: guillaume.wantz@enscbp.fr

Dr. P. Valvin
Laboratoire Charles Coulomb
UMR 5221 CNRS
Université de Montpellier
Montpellier 34095, France

Dr. S. Clevers, Prof. Y. H. Geerts
Faculté des Sciences
Laboratoire de Chimie des Polymères CP 206/01
Université Libre de Bruxelles (ULB)
Boulevard du Triomphe, Brussels 1050, Belgium

Dr. D. Flot
ESRF—The European Synchrotron
71 Avenue des Martyrs, Grenoble 38000, France

The ORCID identification number(s) for the author(s) of this article can be found under https://doi.org/10.1002/aelm.201700218.

DOI: 10.1002/aelm.201700218

 © 2017 WILEY-VCH Verlag GmbH & Co. KGaA, Weinheim

From the induced spectral shifts, various aggregation patterns of the dyes in different media have been proposed. For example, the bathochromically shifted J-bands[7] and hypsochromically shifted H-bands[8] of the aggregates have been explained in terms of molecular exciton coupling theory, i.e., coupling of transition moments of the constituent dye molecules.[9] It is generally agreed that both H- and J-aggregates are composed of parallel dye molecules stacked in a parallel way. A plane-to-plane stacking results in a sandwich-type arrangement (H-aggregates) whereas a head-to-tail arrangement forms J-aggregates leading to 2D dye crystals. Going from a J-aggregation to an H-aggregation will improve the intermolecular overlaps increasing the charge transport properties. Furthermore, since the corresponding total transition dipole moment vanishes, H-aggregates are generally considered as poor emitters.[10] Thus, the aggregation pattern of $\pi$-conjugated oligomers will determine the device performance and/or goal, i.e., OLEDs or solar cells or OFETs.

In this context, we have recently developed a new strategy to tune the optoelectronic properties of an electroactive molecule by simply playing on the modulation of its aggregation.[11] Using the triethoxysilyl function ($Si(OEt)_3$) as a modifiable bulky fragment,[11a] we were able to synthesize highly fluorescent and electroluminescent compound.[11b] After sol–gel hydrolysis, the aggregation of the bisilylated chromophore is modified from J- to H-type (**Figure 1**). The resulting organosilica exhibited decreased electroluminescence but improved photoconductivity.

Following a different approach, Inagaki and co-workers reported photoconductivity on thin films based on periodic mesoporous organosilica (PMO).[12] PMO thin films that possess both visible-light absorption and hole-transporting properties were synthesized from a 4,7-dithienyl-2,1,3-benzothiadiazole-bridged organosilane precursor using polystyrene-*block*-poly(ethylene oxide) (PS-*b*-PEO) as a template. The PMO films exhibited absorption in the visible range between 400 and 650 nm and hole-transport mobilities, estimated by space-charge-limited current, in the order of $10^{-5}$ $cm^2$ $V^{-1}$ $s^{-1}$. They demonstrated that the PMO thin film functions as a p-type layer for organic solar cells by filling an n-type [6,6]-phenyl $C_{61}$ butyric acid methyl ester into the mesopores.

Even if sol–gel chemistry has previously been used to fabricate field-effect transistors (FETs), it has been restricted to the modification of the dielectric layer. On the one hand, pure inorganic coatings such as of $SiO_2$, $HfO_2$, or $TiO_2$, for example, were used as dielectric.[13–15] And on the other hand, hybrids interfacial layer were used to produce high-k hybrid dielectrics for low-voltage organic field-effect transistors.[16] Monosilylated $\pi$-conjugated systems have also been integrated in self-assembled monolayer field-effect transistors.[17–22] In this case, active monolayers have been obtained using the trichloro- or triethoxysilyl functions as the anchoring groups. Electronic conductivity could be measured on thin films of polymerizable liquid-crystalline perylene bisimide bearing a triethylene oxide chain and cyclotetrasiloxane rings.[23,24] Acid-induced in situ polymerization to form siloxane network was demonstrated. In the neutral states, the electrical conductivities of the as-deposited and polymerized thin films were determined to be $1 \times 10^{-10}$ and $2 \times 10^{-10}$ S $cm^{-1}$, respectively.

However, to the best of our knowledge, FETs based on bulk organosilica active layer have never been reported.

Finally, our objective was not only to design and fabricate a hybrid field-effect transistor (HFET) based on a purely organosilylated active layer but also to apply our strategy of the control of the supramolecular organization of the organic part using the inorganic residue. The resulting devices, being completely crosslinked, should exhibit particular stability toward solvent soakings and not only to water as already described in the case of purely hydrophobic organic layer.[25]

We would like to report here, the synthesis and the use of a new sol–gel precursor based on [1]benzothieno[3,2-b][1]benzothiophene (BTBT). Among the numerous conjugated molecules described to date, (BTBT) $\pi$-conjugated systems are actually among the best performing organic semiconductors for use in thin film transistors, as evidenced by record hole ($h^+$) mobilities.[26–28]

The chemistry of BTBT derivatives has been heavily studied. Structural modifications have been performed to finely tune their solubility,[29] their crystallinity,[30–32] their processability,[33] and their stability.[34] Recently, bulky fragments were introduced on the BTBT core in order to control its supramolecular organization. The control has been obtained by balancing between steric hindrance (iPr, tBu, TMS),[35] van der Waals interactions (alkyl),[36] and $\pi$–$\pi$ stacking (phenyl)[34] interactions. More recently, we reported the functionalization of the BTBT core by side chains susceptible to introduce

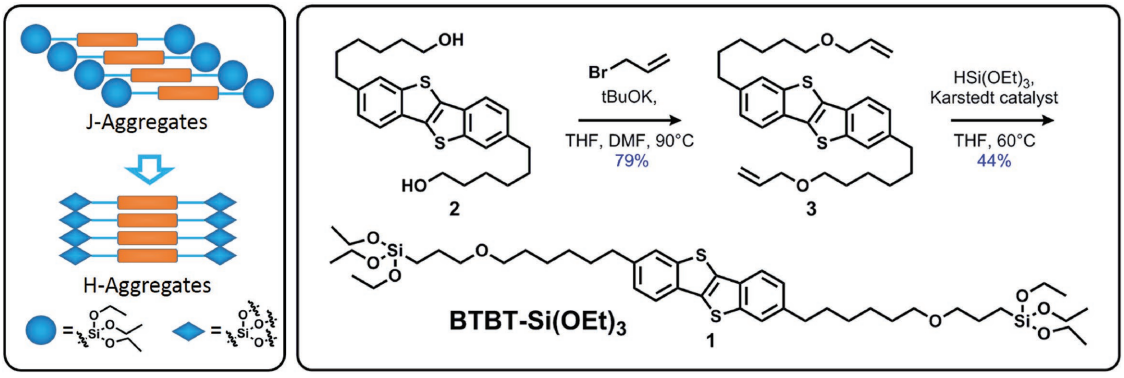


**Figure 1.** Strategy to switch from a J-aggregation to an H-aggregation and synthetic pathway to BTBT-$Si(OEt)_3$ **1**.


© 2017 WILEY-VCH Verlag GmbH & Co. KGaA, Weinheim

stronger interactions such as hydrogen bonds. A rapid and inexpensive functionalization of the BTBT in position 2 and 7 by hexyl chains with hydroxyl groups at their extremities has been developed.[37] This compound **2** (Figure 1) was able to self-organize into a lamellar structure through $\sigma$–$\pi$-stacking and van der Waals interactions but also through hydrogen bonding interactions. The hydrogen-bonded network controls the interlamellar region in terms of organization and stability. Thermally evaporated **2**-based OFETs exhibited good mobilities up to 0.17 $cm^2\ V^{-1}\ s^{-1}$ measured under inert atmosphere but also in ambient air. Thus, this diol derivative constitutes a very promising platform for the design of a new functionalized BTBT sol–gel precursor (**1**). Functionalization of this BTBT derivative by triethoxysilyl functions will not only help us to apply our strategy to control its supramolecular organization but should also allow the fabrication of very homogeneous thin film by wet process and extremely stable thin films stabilized by siloxane network resulting from the hydrolysis–polycondensation process.

BTBT-Si$(OEt)_3$ **1** has been processed in field-effect transistors using a hydrolysis–polycondensation sequence. Devices exhibited decent charge transport properties according to its hybrid nature with $\pi$-conjugated pathways but also a non-negligible volume fraction of condensed silicon oxide moieties. Attention has been paid to optimize the processing conditions in order to achieve a fully covalent approach in such HFETs. Molecules were covalently bonded to each other, but also covalently attached to the gate dielectric (silicon oxide) as well as covalently bonded to the gold electrodes thanks to the use of an appropriate self-assembled monolayer. HFETs showed impressive resilience against polar, aliphatic and aromatics solvents even under sonication. This study opens the route toward a new class of hybrid materials to create highly robust electronic applications. This work constitutes the first description of a hybrid field-effect transistor based on an organosilica active layer.

## 2. Results and Discussion

### 2.1. Synthesis

The sol–gel precursor **1** (BTBT-Si$(OEt)_3$) was obtained in two steps from bis(hydroxy–hexyl)-BTBT(BHH-BTBT) **2**. Alkylation of the hydroxyl functions with allylbromide followed by a hydrosilylation of the resulting allyl functions offered **1** with an overall yield of 35% after purification on silica gel. This new sol–gel precursor is highly soluble in common organic solvents and thermally stable up to 360 °C with a melting point as low as 42 °C (Figure S7, Supporting Information).

### 2.2. Organization of the Precursor 1 (BTBT-Si$(OEt)_3$)

Single crystals of **1** could be obtained by crystallization at low temperature below 9 °C (Figure S7b, Supporting Information). Thin colorless plates were obtained upon cooling a solution of **1** in dry ethanol. Ethanol was used to avoid trans-esterification of the triethoxysilyl functions. Crystals obtained were suitable to record microdiffraction patterns at the Microfocus Beamline ID23-2 (European Synchrotron Radiation Facility – ESRF, Grenoble). **1** crystallizes in a triclinic system with a P-1 space group. One independent molecule constitutes the asymmetric unit (**Figure 2**).

As attested by the single crystal structure, the crystallization of BTBT-Si$(OEt)_3$ afforded a perfectly flat molecule (Figure 2b) with the lateral chains in the same plane as the BTBT core. This conformation and the steric hindrance introduced by the triethoxysilyl units result in a J-type organization of **1** in the solid state (**Figure 3**). In the crystal, J-stacks are organized in layers separated by the triethoxysilyl functions along the *c*-axis with a *d*-spacing of 22.17 Å.

Upon deposition by spin-coating of a film of **1** from a chloroform solution on a glass plate, two different behaviors could

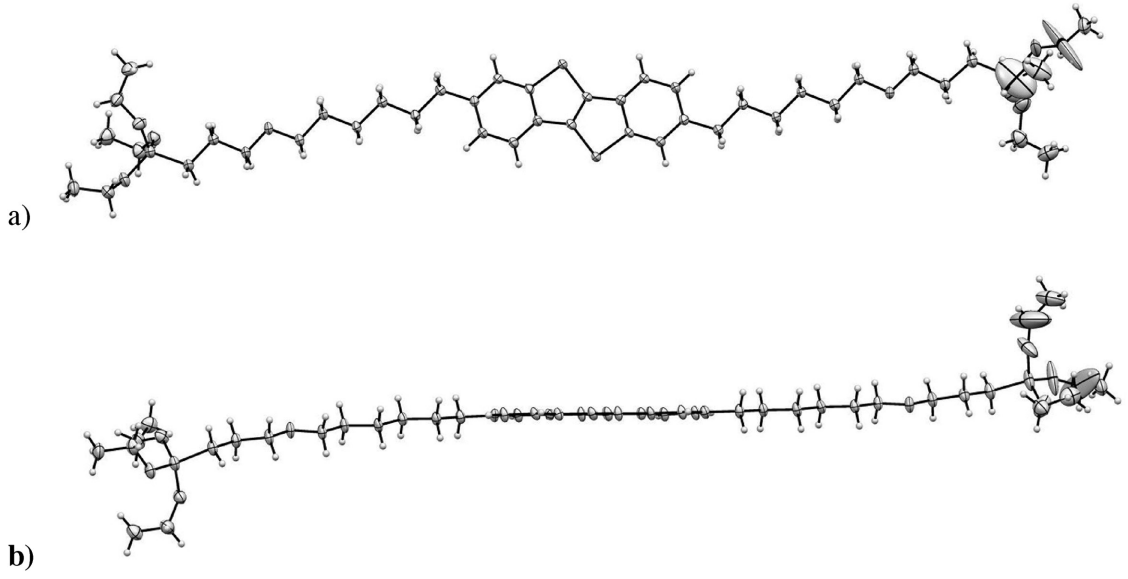


**Figure 2.** Crystal structure recorded on a single crystal of **1**: anisotropic displacement parameters are drawn at the 50% probability level. a) Front view and b) side view of the molecular unit.


© 2017 WILEY-VCH Verlag GmbH & Co. KGaA, Weinheim

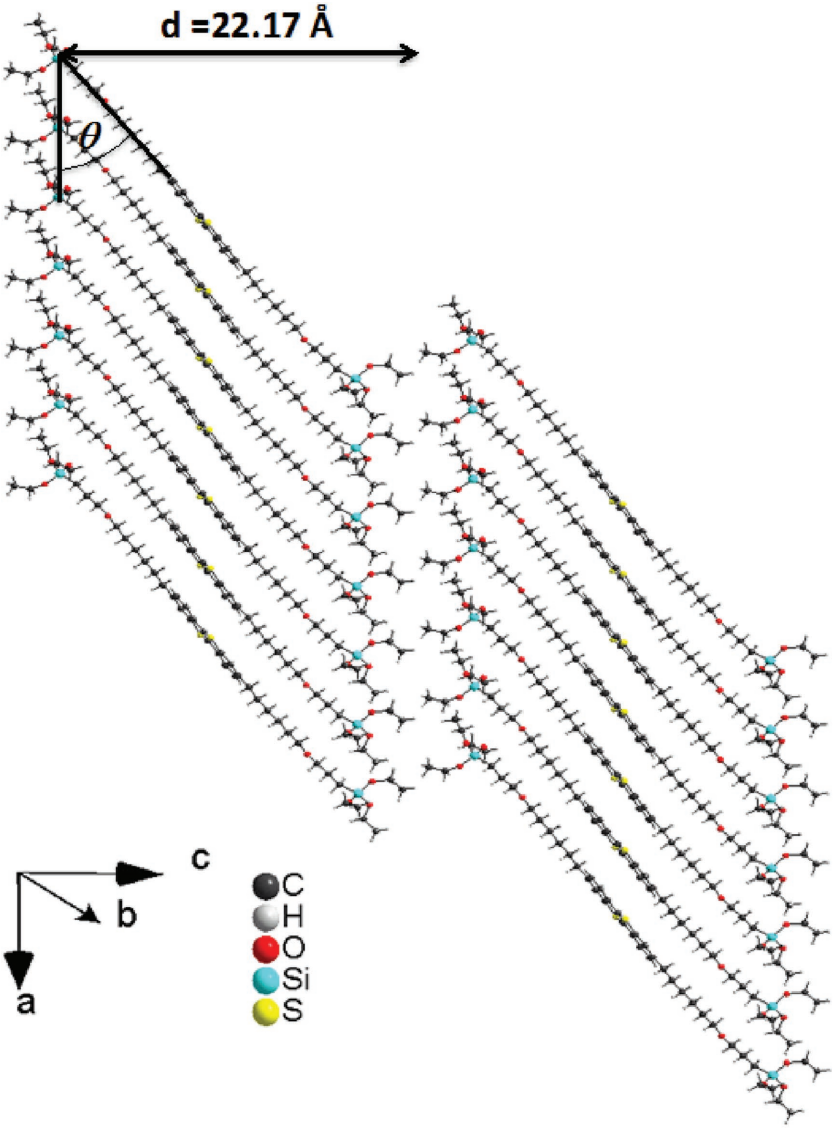


**Figure 3.** Packing arrangement of **1**: J-stacks running along the *a*-axis with a slip angle $\theta$ of 32.5° and organized in layers along the *c*-axis with a *d*-spacing of 22.17 Å.

be identified. (**Figure 4**) The absorbance properties of **1** were first transfer from the solution to the viscous amorphous state (state I). Then a few minutes after drying, the thin film started to crystallize (state II, $\mathbf{1}_{crst}$) at room temperature with a speed estimated at 1.7 mm $min^{-1}$ (see **Figure 5**c and the Supporting Information for movies).

The absorbance maximum was red shifted from 331 to 342 nm during this state I to state II modification (cf. Figure 5a). In a same way, the emission properties of **1** in the thin film evolved during its crystallization (Figure 5b). The emission band was not only blue shifted from 380 to 370 nm but also its intensity dramatically increased by about one order of magnitude from 40 to 120 s. The red shift in absorbance maximum and increased fluorescence intensity are consistent with an exciton coupling of the aromatic units due to the formation of J-aggregates during the crystallization of **1** in the thin film agreeing with the steric hindrance introduced by the triethoxysilyl fragments.

This behavior is supported by X-ray diffraction diagrams of **1** (**Figure 6**). X-ray diffraction diagrams of **1** as powder ($\mathbf{1}_{powder}$), as a thin film ($\mathbf{1}_{crst}$) and generated from the single crystal structure ($\mathbf{1}_{single\text{-}crystal}$) are displayed. The powder X-ray diffraction (PXRD) diagram of $\mathbf{1}_{powder}$ is composed of a series of small angle reflexions {$2\theta$ = 3.89° (22.70 Å), 11.66°, and 15.47°} corresponding to a lamellar structure close to the one observed in the single crystal lattice with an interlayer distance (*d*-spacing) calculated from these reflections of 22.17 Å. As in the case of the generated diffractogram, the (002) reflexion is absent on the PXRD diagrams. Offsets observed between reflexion peaks on $\mathbf{1}_{powder}$ and $\mathbf{1}_{single\text{-}crystal}$ could be due to different temperature of measurements. $\mathbf{1}_{powder}$ was recorded at room temperature while the single crystal structure was measured at 100 K. $\mathbf{1}_{crst}$ exhibited also a well-ordered structure after crystallization as indicated by X-ray diffraction measurements (Figure 6, blue curve). A series of peaks assignable to (001) is also clearly visible up to the (007) reflection. Once again, the (002) reflexion is absent. We can reasonably affirm that the precursor exhibits the same lamellar structure in all cases. However,

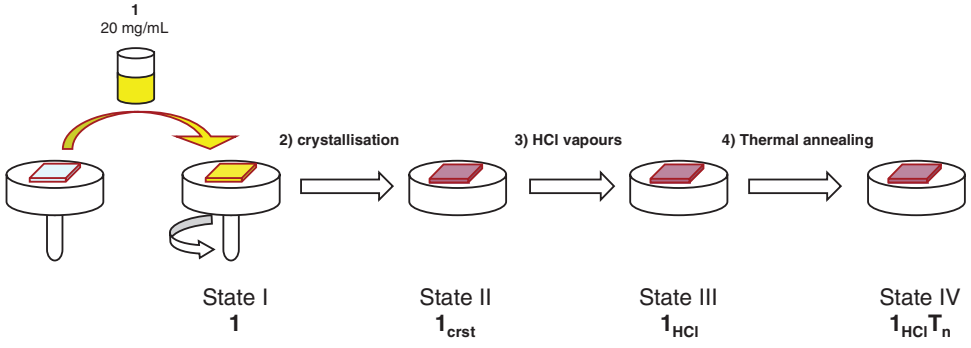


**Figure 4.** Deposition and hydrolysis–polycondensation process of **1** in thin film.


© 2017 WILEY-VCH Verlag GmbH & Co. KGaA, Weinheim

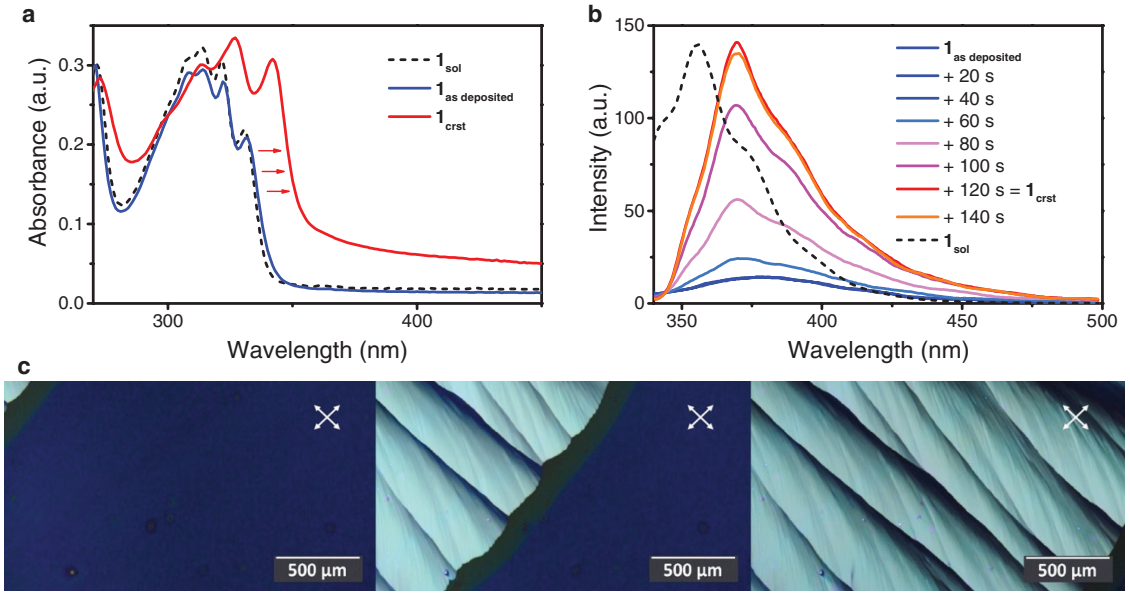


**Figure 5.** Optical properties of **1**. a) Absorption spectra of **1** in $CHCl_3$ ($\mathbf{1}_{sol}$) and as a thin film on a glass plate before (**1**) and after its crystallization ($\mathbf{1}_{crst}$). b) Emission spectra of **1** as a thin film on a glass plate before and during its crystallization (see Figure 7b). $\mathbf{1}_{sol}$ curve was normalized to $\mathbf{1}_{crst}$ intensity for better comprehension). c) Thin film crystallization under cross-polarized light, from the left to the right (movies showing the crystallization of **1** thin film in the Supporting Information).

differences in high angle reflexions (low distances) observed in $\mathbf{1}_{powder}$ and $\mathbf{1}_{crst}$ suggest that the organizations of the molecules within layers could differ as in polymorphs. The absence of reflections at high angle in the thin film is attesting of a preferred orientation of the lamellar structure parallel to the substrate. The thin film structure is, thus, favorable to charge transport.

### 2.3. Hydrolysis–Polycondensation

Hybrid materials are obtained by the hydrolysis–polycondensation of the sol–gel precursor in the thin film state.

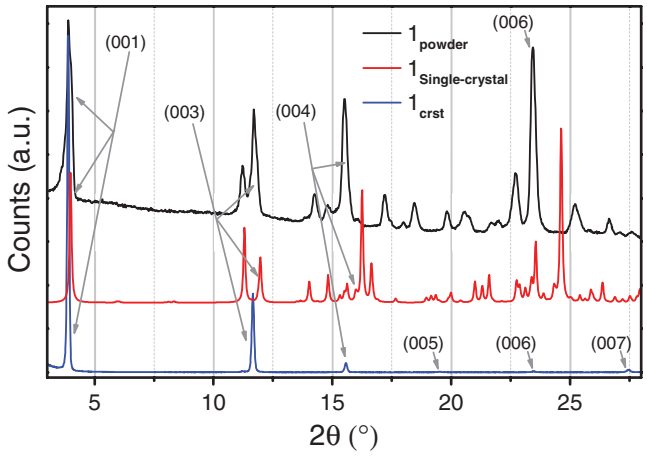


**Figure 6.** X-ray diffractograms comparison: as a powder ($\mathbf{1}_{powder}$, black line), calculated diffraction profile from the single crystal structure ($\mathbf{1}_{single\text{-}crystal}$, red line), as a thin crystallized film ($\mathbf{1}_{crst}$) obtained by spin-coating from a $CHCl_3$ solution (blue line).

An acid, a base, or a nucleophile can catalyze the reaction. After drying and crystallization of a pure thin film, $\mathbf{1}_{crst}$ is exposed to hydrochloric acid vapors (Figure 4, state III). The contribution of the hybrid network formation was revealed by the comparison of thin films obtained from $CHCl_3$ solutions of **1** before and after HCl vapors exposure followed by a thermal annealing at 150 °C. Hybrid films will be noted $\mathbf{1}_{HCl}$. Films, subsequently thermally annealed at 150 °C for *n* hours, will be noted $\mathbf{1}_{HCl}\boldsymbol{T}_n$.

The hydrolysis–polycondensation process could be monitored by infrared spectroscopy (**Figure 7**). During this chemical modification, the ethoxy groups of **1** are eliminated while Si—OH and Si—O—Si bonds are created. This transformation can be monitored from the band intensity of the asymmetric ($\nu_{as}CH_3$) and symmetric ($\nu_sCH_3$) stretching vibrations of the $CH_3$, respectively, at 2972 and 2882 $cm^{-1}$. On the fourier transform infrared spectroscopy (FTIR) spectrum of $\mathbf{1}_{HCl}$, right after HCl exposure, the intensity of these vibrations is lowered which is significant of the hydrolysis of Si—OEt bonds. The fast hydrolysis of triethoxysilyl functions is also attested by the apparition of a broad band ranging from 3100 to 3580 $cm^{-1}$ and corresponding to the stretching of the O—H bonds ($\nu$O—H) formed during the hydrolysis. In a same way, the formation of the Si—O—Si network can be followed by the decrease of the band intensity of the asymmetric ($\nu_{as}$Si—O—$CH_2$) and symmetric ($\nu_s$Si—O—$CH_2$) stretching vibrations of the Si—O—$CH_2$ bond, respectively, observed at 1106 and 1083 $cm^{-1}$, the stretching vibration of the $CH_2$—O—Si bond ($\nu CH_2$—O—Si) at 1168 $cm^{-1}$, the deformation of the Si—O—$CH_2$ ($\delta$Si—O—$CH_2$) at 957 $cm^{-1}$, and the deformation of the $CH_2$ ($\delta CH_2$) at 780 $cm^{-1}$. The appearance of a two broad bands from 1100 to 1033 $cm^{-1}$ and from 910 to 890 $cm^{-1}$ corresponding, respectively, to the stretching ($\nu$Si—O—Si) and the deformation ($\delta$Si—O—Si)


© 2017 WILEY-VCH Verlag GmbH & Co. KGaA, Weinheim

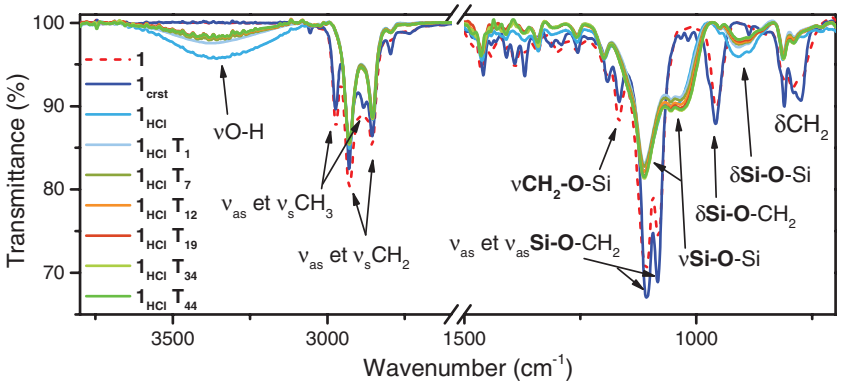


**Figure 7.** Infrared spectra of thin films: precursor **1**, after crystallization $\mathbf{1}_{crst}$, after exposure to HCl vapor $\mathbf{1}_{HCl}$ and after *n* hours of thermal annealing $\mathbf{1}_{HCl}T_n$. All films are deposited on silicon wafers.

vibrations of the various Si—O—Si bonds of the silicate network is attesting of the condensation.

During the thermal annealing at 150 °C, the condensation rate is clearly increasing as attested by a decrease in the intensity of the *ν*O—H and a small increase in the intensities of the different vibrations of the Si—O—Si bonds.

### 2.4. Optical Properties of the BTBT Core in the Precursor and in the Organosilica

The most important modification of the optoelectronic properties of the condensed organosilica network concerns its emission properties (**Figure 8**b). In a first step, going from **1** as a crystallized film ($\mathbf{1}_{crst}$) to **1** exposed 2 min to HCl vapors ($\mathbf{1}_{HCl}$), causes a decrease in the fluorescence intensity of the 370 nm emission band. The hydrolysis of the bulky triethoxysilyl groups to produce smaller trihydroxysilyl groups certainly results in a first contraction of the network improving intermolecular interactions between the BTBT cores and quenching the fluorescence. This contraction of the network during the hydrolysis–polycondensation could be experimentally evidenced by measuring the profile of a scratch done in a thin film $\mathbf{1}_{crst}$ (Figure S8, Supporting Information). In this case, before hydrolysis–polycondensation (Figure S8, blue curve, Supporting Information) the thickness of a film $\mathbf{1}_{crst}$ is 184 ± 3 nm and decreased to 164 ± 3 nm just after the exposure to HCl vapors ($\mathbf{1}_{HCl}$) (Figure S8, $\mathbf{1}_{HCl}$ green curve, Supporting Information).

However, the emission maximum remained located at 370 nm meaning that the J-aggregation is conserved after the hydrolysis (Figure 8b, spectrum $\mathbf{1}_{HCl}$). The structural modifications due to the condensation of the silanol induced by the thermal annealing prove to influence more dramatically the optical properties (Figure 8b, spectra $\mathbf{1}_{HCl}T_n$). In this case, the emission band observed at 370 nm on the $\mathbf{1}_{HCl}$ spectrum, decreased in the benefit of a new emission at 442 nm. The thickness of the film being unchanged (165 ± 3 nm) during the thermal annealing (Figure S8, $\mathbf{1}_{HCl}T_{44}$, red curve, Supporting Information). This could result from the anticipated transition of the J-aggregation to the H-aggregation.

The above optical behavior could be explained by the excitonic coupling theory of Kasha and co-workers,[38] which describes the excitonic interaction of the transition dipole moments of chromophores with respect to their geometrical arrangement as a point dipole approximation (**Figure 9**).

In organized solids or thin films as it is the case here, exciton states, or collective excited states can arise, and are not a simple superposition of the excited states of the free molecules. In this case, for parallel-aligned dimers the optical excitation is only allowed from the ground state to one of the two excitonic states depending on the slip angle *θ*. For $\theta < 54.78°$ the lower energy state is allowed (leading to a bathochromically shifted J-band), while for $\theta > 54.78°$ the allowed state is at higher energy (leading to a hypsochromically shifted H-band). In a same way, according to Kascha's rules, fluorescence emission can only originate from the low energy level.

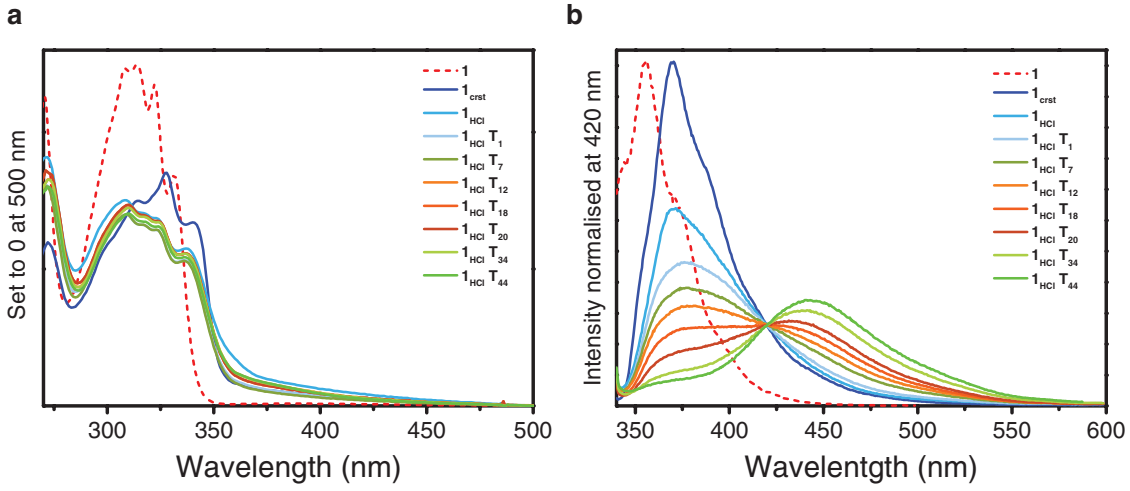


**Figure 8.** a) UV–vis and b) emission spectra of films of **1**, $\mathbf{1}_{crst}$, $\mathbf{1}_{HCl}$, and $\mathbf{1}_{HCl}T_n$ on glass with $T = 150$ °C. **1** curve is normalized to $\mathbf{1}_{crst}$ intensity for better comprehension.


© 2017 WILEY-VCH Verlag GmbH & Co. KGaA, Weinheim

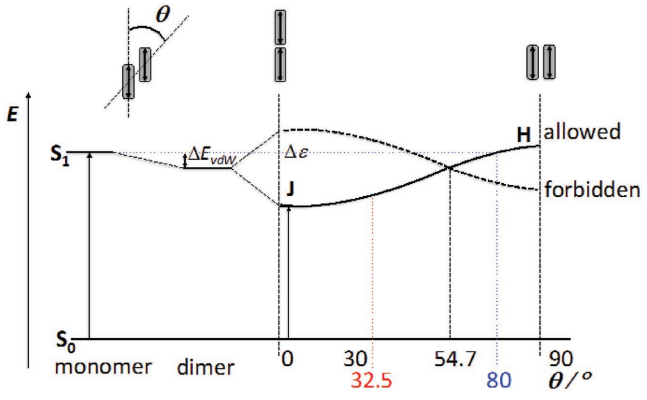


**Figure 9.** A schematic energy diagram for aggregated dimers with coplanar inclined transition dipoles. $\Delta E_{vdW}$ = difference in van der Waals interaction energies between ground and excited states.

The slip angle $\theta$ could be obtained from the single crystal structure of **1** (Figure 3). With a value of 32.5° < 54.78°, the J-aggregation in **1** as crystal and $\mathbf{1}_{crst}$ as a crystallized film is confirmed.

In the case of J-aggregates, fluorescence occurs from the low-energy band and is thus moderately red-shifted (+14 nm from **1** to $\mathbf{1}_{crst}$, Figure 8b). Absorption and emission arising from the same low-energy allowed transition, the fluorescence is fast and intense (see **Figure 10**, $\tau_1$ = 202 ps (±15 ps) and Figures S10–S12 in the Supporting Information for a description of the time resolved fluorescence measurements). On the other hand, the H-aggregate excitonic splitting gives a high-energy allowed transition and a low-energy forbidden band. Absorption is dominated by the high-energy band, but the fluorescence occurs from the low-energy band and is thus strongly quenched, red-shifted (+86 nm from $\mathbf{1}_{HCl}$ to $\mathbf{1}_{HCl}T_{44}$, Figure 8b) and has a long-life (Figure 10, $\tau_{\mathbf{1}HClT44}$ = 774 ps (±120 ps). As already deduced from its emission spectrum (Figure 8b, spectrum $\mathbf{1}_{HCl}$), an intermediate situation is expected for $\mathbf{1}_{HCl}$. With a τ of 314 ps (±20 ps) close to the one of $\mathbf{1}_{crst}$, BTBT cores are clearly still in a J-configuration with a small contraction of the network due to the lost of the steric hindrance introduced by the triethoxysilanes.

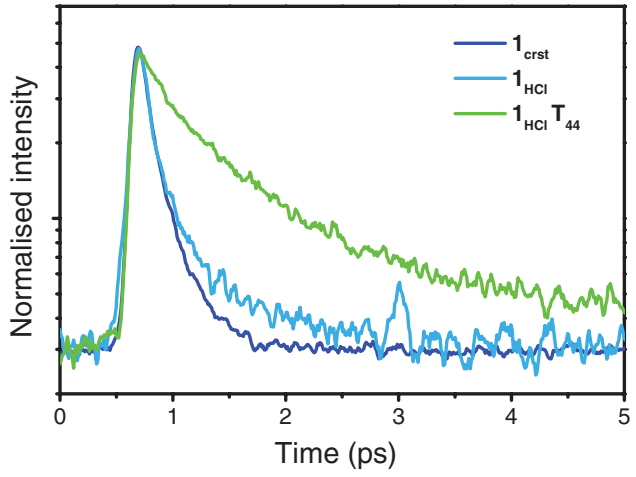


**Figure 10.** Time resolved emission intensity of films of $\mathbf{1}_{crst}$, $\mathbf{1}_{HCl}$, and $\mathbf{1}_{HCl}T_{44}$ on glass (see the Supporting Information for a description of the time resolved fluorescence measurements).

However, two observations need to be stressed. On the one hand, the UV–vis absorbance, after hydrolysis, is quickly shifted to a maximum close to the isolated molecule $\mathbf{1}_{sol}$ (a few nm difference) while a more significant shift could be expected. This is indicating that the resulting slip angle $\theta$ is closer from 80° than 90°. For example, in Figure 9, an angle slip of 80° would give the same transition as in the monomer. On the other hand, unlike theoretically expected, the UV–vis absorbance does not evolve during the thermal annealing. The red shifting of the emission during annealing could be the result of a dimerization along the H-stacks conducting to an emission from exciton states of excimers as already observed by Chen et al.[39]

Even if the evolution of the optical properties of the $\mathbf{1}_{crst}$ thin film before and after hydrolysis–polycondensation showed clearly that the supramolecular organization of the BTBT core shifted from a J-aggregation to an H-aggregation, constraints imposed by the Si—O—Si bonds formation resulted in a lost of the long range organization (see Figure S13 in the Supporting Information). As already mentioned, upon deposition by spin-coating of a film of **1** from a chloroform solution on a glass or silicon plate, the thin film started to crystallize to self-organize according to a lamellar structure with an interlayer distance $d1$ = 22.7 Å calculated from series of small angle reflexion ($2\theta$ = 3.89°), with a preferred orientation of the lamellar structure perpendicular to the substrate. Exposed to HCl vapors, the sharp diffraction peaks disappeared to leave a very large peak located at $2\theta$ = 5.02° corresponding to a contraction of the lamellar structure with a $d$-spacing of $d2$ = 17.48 Å (Figures S13 and S14, Supporting Information). This could be the result of the elimination of the ethoxy functions and a beginning of the Si—O—Si bond formation. After thermal annealing even if we showed by FTIR that the condensation was optimized and by emission spectroscopy that the H-aggregation was installed, the diffraction peak remained at a small angle of $2\theta$ = 5.17° corresponding to a $d$-spacing of $d3$ = 17.07 Å. that is much smaller than the 34 Å corresponding the length of a molecule. In this case, the alkyne chains have been certainly tilted to optimize $\pi$–$\pi$ stacking between the BTBT cores in the H-aggregates (Figure S14, Supporting Information).

### 2.5. Hybrid Field-Effect Transistors

The energy levels of **1** have been characterized by absorption spectroscopy and cyclic voltammetry (see Figure S15 in the Supporting Information). With an absorption edge of 339 nm in chloroform and an oxidation potential onset of 0.75 V versus ($Fc/Fc^+$), **1** optoelectronically behaves as most of CnBTBTCn.[27] The optical band gap is evaluated at 3.66 eV, the highest occupied molecular orbital (HOMO) and the lowest unoccupied molecular orbital (LUMO) levels are located at –5.6 and –1.9 eV.

Considering the good structuration of its thin films and its suitable optoelectronic properties, **1**-based HFET has been fabricated and characterized on prepatterned gold bottom contacts, bottom gate structures on heavily doped silicon substrates (see experimental details in the Supporting Information). The gate dielectric is a 230 nm thick thermally grown silicon oxide


© 2017 WILEY-VCH Verlag GmbH & Co. KGaA, Weinheim

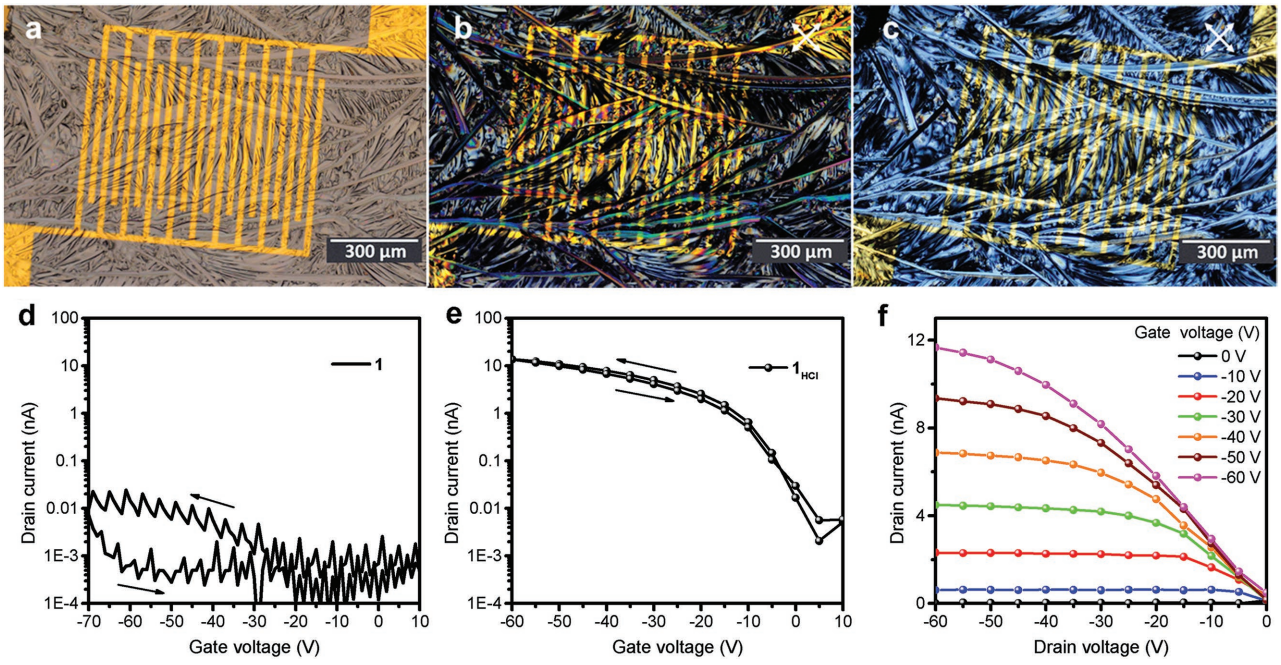


**Figure 11.** a) Optical microscopy pictures of a crystalline film of $\mathbf{1}_{crst}$ on an OFET before exposure to HCl vapors and b) cross-polarized; c) cross-polarized picture of the subsequent film after HCl exposition (drain–source Au-electrodes can be seen through the transparent hybrid film). Transfer characteristics of a spin-coated **1**-based OFET in saturated regime at $V_{DS} = -60$ V before and after sol–gel chemistry: (c) $\mathbf{1}_{crst}$ and d) $\mathbf{1}_{HCl}$, respectively, and e) $\mathbf{1}_{HCl}$ corresponding output characteristics for different gate voltages.

($SiO_2$). A 20 mg $mL^{-1}$ solution of **1** in chloroform was spun resulting in thin films with a thickness of around 100 nm.

As expected, **1** formed crystalline thin films on the chips as attested by the birefringence observed by polarized optical microscopy (POM) in **Figure 11**b. The birefringence remained after exposure to HCl vapors signifying that certain degree of organization has been conserved (Figure 11c). Transistors were electrically characterized at each fabrication steps. As previously deduced from their absorption and emission properties, after crystallization but before exposure to HCl vapors, the BTBT core are organized according to a J-aggregation in $\mathbf{1}_{crst}$ thin film. This supramolecular organization is unfavorable to charge transport. As a result, no field-effect transistor signal could be measured (Figure 11d). After HCl exposure, the transition from a J-aggregation to an H-aggregation started and even if the transition is not fully accomplished, the BTBT-cores are getting closer from each other's in the $\mathbf{1}_{HCl}$ thin film. The transistors start to operate normally. Transfer and output characteristic with negligible hysteresis are measured. The ON/OFF ratio is in the order of $10^3$ (Figure 11e, $1_{HCl}$). The hole mobility was evaluated at $1.7 \times 10^{-6}$ and $2.41 \times 10^{-6}$ $cm^2$ $V^{-1}$ $s^{-1}$ in linear and saturation regimes, respectively (Figure 11e, $1_{HCl}$). Such values are low compared to classical organic semiconductors as explained by the chemical nature of the hybrid material, composed of a large volume of silicon oxide moieties ($SiO_x$ sublayers) well known as an electrically insulating material. However, it is important to highlight that crosslinked networks here are providing remarkable operational field-effect transistors. After thermal annealing at 150 °C for 44 h, the transition from J- to H-aggregation was definitively established. Nevertheless, such a harsh treatment significantly decreased the drain currents by one order of magnitude (Figure S16c, Supporting Information). Resulting mobilities were then in the range of $2.0 \times 10^{-7}$ $cm^2$ $V^{-1}$ $s^{-1}$. Thinking that 150 °C was too high to avoid stress arising from the contraction of organosilica thin film and knowing that silicon oxide and organosilica do not exhibit the same thermal dilatation coefficient, we managed to realize the J to H transition under mild conditions (70 °C). The transition was followed by emission spectroscopy (see Figure S17a,b in the Supporting Information) and completed after 30 d at 70 °C in ambient air. Following this procedure, electronic properties were retained even after 30 d at 70 °C (Figure S17d, Supporting Information). Indeed mobilities in saturated regime evolved from $2.4 \times 10^{-6}$ to $5.2 \times 10^{-6}$ $cm^2$ $V^{-1}$ $s^{-1}$ after annealing. The mobility remained of the same order of magnitude and an unexpected shift of the threshold voltage to the negatives values was observed that could be due to increased charge traps density. Our results suggest that a complete polycondensation thanks to annealing is not necessary to achieve operational transistors. Only a slight mobility increase is observed at this stage. However, the complete polycondensation improved significantly the stability of the devices as discussed in the following part.

The fabrication process of those HFETs includes a drastic thermal annealing in air (70 °C, 30 d). Therefore, one can already suggest that they are highly stable. The interest of the triethoxysilyl function is that the hydrolyzed-polycondensed active layer is crosslinked and therefore should be very stable. The other advantage is that the active layer is directly grafted on the insulating silicon oxide by Si—O covalent bonds. As a result, the active layer should be extremely stable without any possibility of solubilization or delamination despite solvent washings


© 2017 WILEY-VCH Verlag GmbH & Co. KGaA, Weinheim

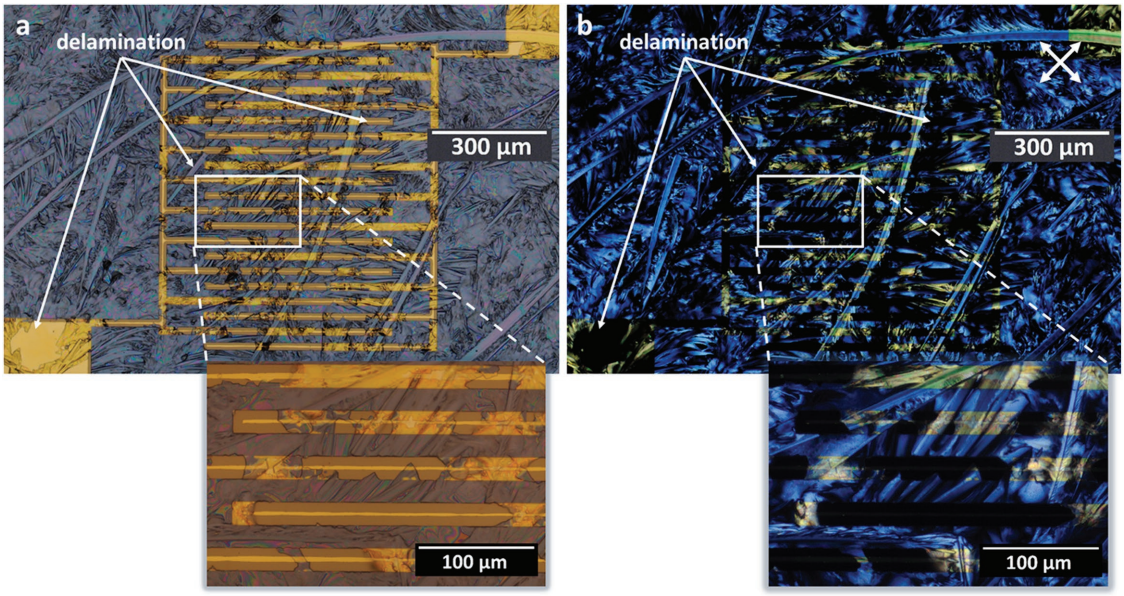


**Figure 12.** a) Uncrossed and b) cross-polarized optical microscopy pictures of the delamination of the hybrid film from the gold electrodes after washing with a water/methanol mixture under sonication.

or sonication treatments. However, closer observations of solvent washed devices revealed a problem arising from the gold electrodes (Au) and the organosilica interface (**Figure 12**). Although it is difficult to see the absence of the hybrid film on the electrode under nonpolarized light, using POM clearly reveals black areas on the Au electrodes. In the absence of covalent bond with the gold surface, the hybrid film has been peeled off the electrodes during the washing by a methanol/water mixture (50 MeOH/50 $H_2O$) under ultrasonication. Under pure water washing this phenomenon does not occur.

To solve this problem, we pretreated the gold electrodes with an interface monolayer, (3-mercaptopropyl)triethoxysilane (MTES). This surface agent is able to covalently bind to gold and to the organosilica. On the one hand, it binds to gold by the thiol function and on the other hand, it binds to the organosilica by the triethoxysilyl function during sol–gel process (Figure S18, Supporting Information). Grafting of the thiol function on the gold electrodes was followed by X-ray photoelectron spectroscopy (XPS) (Figure S19, Supporting Information). First of all, the apparition of the S 2p doublet at 161.9 and 163.1 eV on sample functionalized with MTES clearly indicates that the MTES has been efficiently grafted on the gold surface which is consistent to literature.[40,41] No unfixed thiol signal around 165 eV was observed,[40] which proves that the grafting was complete and the rinsing was enough to remove the excess of interface agent. Additionally, the grafting of the MTES was supported by the apparition of an additional component on the C 1s signal at 286.5 eV corresponding to C—O bonds, as well as the apparition of an O 1s signal at 532.1 eV and a Si 2p signal at 102.7 eV, which all come from the triethoxysilyl moieties. The C 1s signal originating from C—C of the hydrocarbon pollution usually observed on gold could be observed on gold reference at 284.2 eV. The width of the corresponding peak on the gold treated with the MTES was significantly increased attesting the presence of the supplementary C—S and C—Si bonds brought by the interface agent. However, spin-coating of **1** on top of the MTES functionalized gold patterns was unsuccessful due to dewetting of **1** on the surface (**Figure 13**a). This case differs from the delamination previously observed. Here, the organosilica is not formed; this is just an adhesion issue of **1** on the grafted gold surface. To overcome this dewetting issue, after having grafted the MTES on the gold electrodes, a prehydrolysis by HCl vapors of the resulting monolayer triethoxysilyl groups is necessary before to deposit the precursor **1** (Figure 13b). Consequently, the grafted gold becomes hydrophophilic thanks to a monolayer of (3-mercaptopropyl)trihydroxysilane.

On XPS spectra, after HCl treatment of grafted gold (Figure S19b, Supporting Information) one can clearly see the C—O signal disappearance confirming the hydrolysis of the triethoxysilyl functions, being in good agreement with literature.[42] This is also confirmed by a broadening of the O 1s signal after HCl exposure which could arise from the combination of the signals coming from the Si—O—Si and Si—OH signal which should appear around 531.4 and 532.3 eV.[43,44] This result is a strong indication that not only the MTES has been efficiently grafted on the gold surface but also that the triethoxysilyl functions have been entirely converted into Si—OH or Si—O—Si after exposure to HCl vapors. With this procedure, the gold electrode bears —OH function at its surface to improve the wettability of the organic precursor as well as providing functionalities to create covalent bonds between the electrode and the hybrid sol–gel semiconductor. As a result, after prehydrolysis of the agent grafted on gold, **1** spreads perfectly on the hydrolyzed grafted-Au surface (Figure 13b). By this way the process could be completed (see Figure 13c). The achieved HFET are described in Figure S18 (Supporting Information).

Resulting devices obtained with the complete process were successively soaked into various solvents during an hour without sonication or during 2 min under sonication. In those two cases, the hybrid film remained perfectly stable without


© 2017 WILEY-VCH Verlag GmbH & Co. KGaA, Weinheim

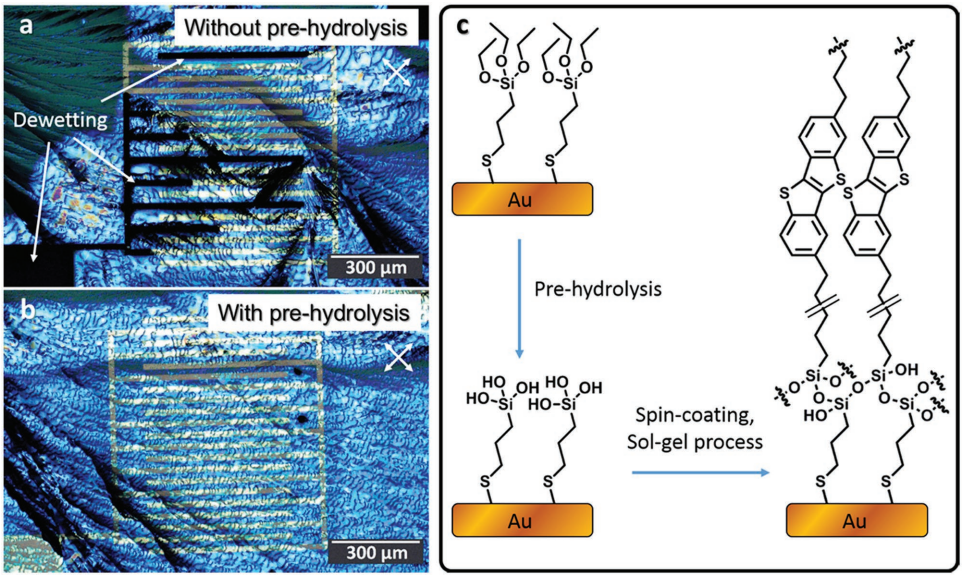


**Figure 13.** Cross-polarized pictures of $\mathbf{1}_{crst}$ deposited by spin-coating on a FET with electrodes covered with a MTES monolayer showing: a) the dewetting (black area on the gold pattern) from the grafted gold during the process without prehydrolysis of the MTES monolayer and b) homogeneous deposition on the substrate submitted to a prehydrolysis of the MTES monolayer by HCl vapors before the deposition. c) Schematic depicting the evolution of the surface of the gold electrodes during the new fabrication process of the HFET incorporating the MTES as interlayer agent.

any delamination at the $\mathbf{1}_{HCl}$–Au interface (**Figure 14** and Figure S22 (Supporting Information)) thanks to the interface grafting agent affording covalent bonding of the hybrid materials onto the gold electrode.

After each soakings (see Figure S20 in the Supporting Information for procedure) transfer and output curves were recorded. Mobilities were also extracted from linear and saturation regimes (**Figure 15** and Figure S21 (Supporting Information)). All devices maintained their electrical properties with average mobilities ranging from $5 \times 10^{-6}$ to $1 \times 10^{-5}$ cm$^2$ V$^{-1}$ s$^{-1}$ after successive solvent washings of an hour with no significant trend. Similar solvent resilience was observed upon successive ultrasonication for 2 min (see Figures S22 and S23 in the Supporting Information). These observations proved that the different solvents were not affecting chemically the HFET and thus their electrical performances. It is worth noting that a complete

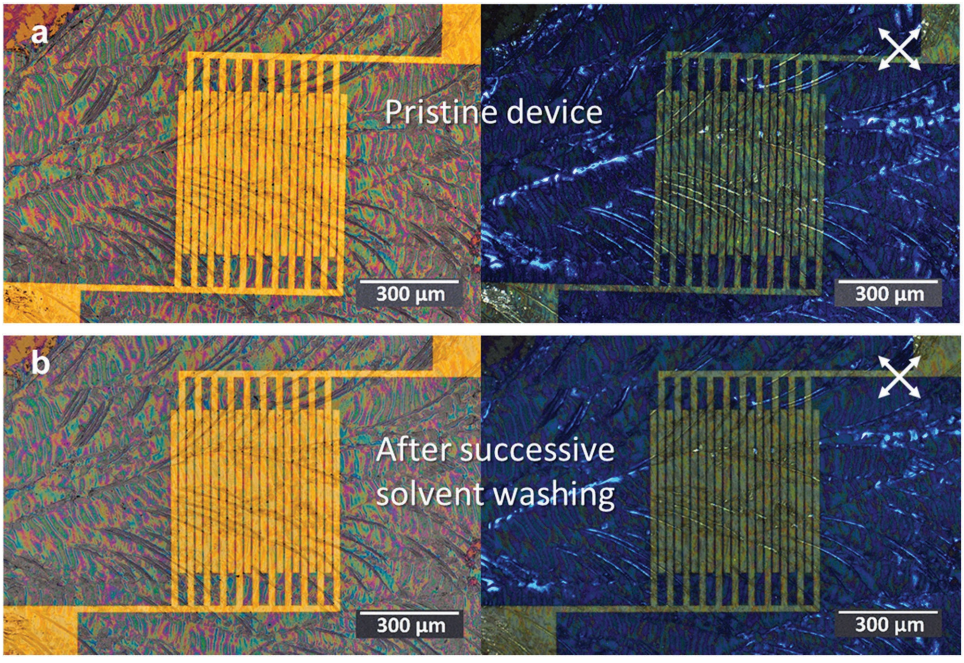


**Figure 14.** Uncrossed and cross-polarized pictures of $\mathbf{1}_{HCl}$ annealed-based HFET embedding the MTES monolayer showing: a) the pristine hybrid film, b) after five successive solvent washings of an hour in the following order: pentane, $H_2O$/MeOH, $CHCl_3$, THF, and toluene.


© 2017 WILEY-VCH Verlag GmbH & Co. KGaA, Weinheim

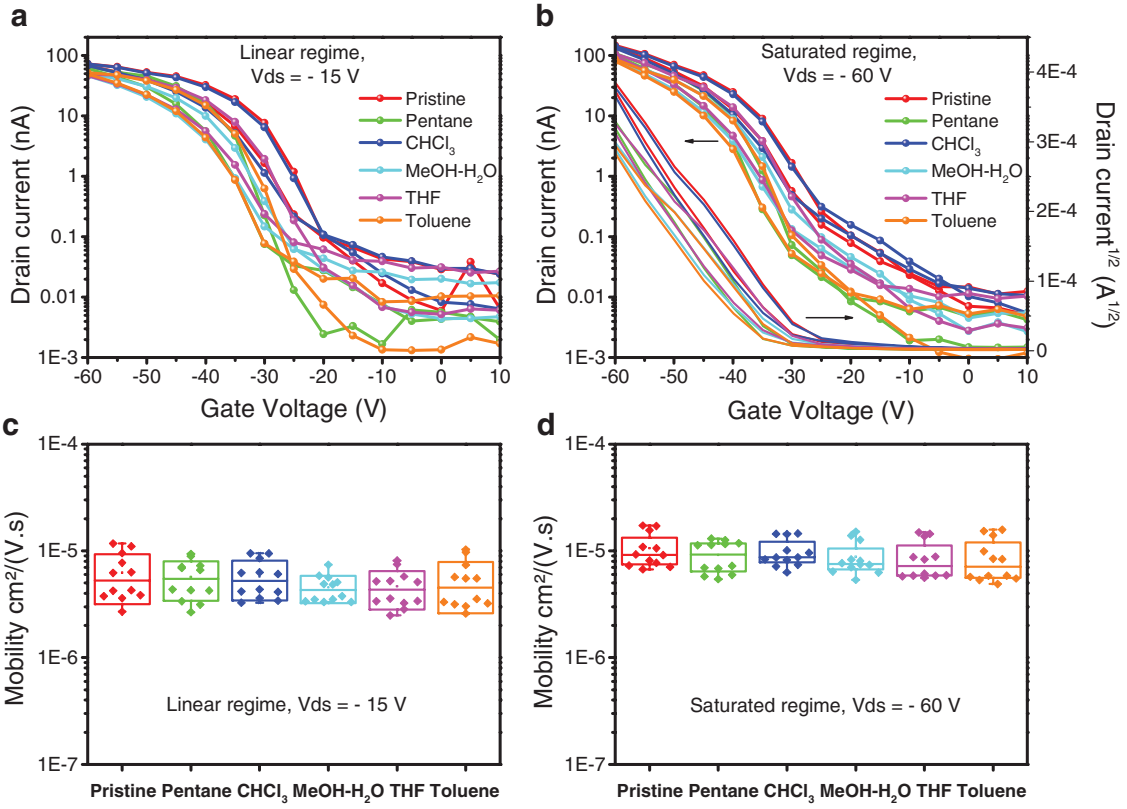


**Figure 15.** Transfer curves in a) linear and b) saturated regime, respectively, before and after 1 h successive washing in each solvent with c,d) their respective mobility values.

polycondensation is required to obtain a strong solvent resilience. Devices that were not thermally annealed, i.e., not fully converted from J to H do not exhibit such a good stability in toluene, for instance (Figure S25, Supporting Information).

## 3. Conclusion

For the first time, we report the design of HFETs. Those devices are based on organosilicas incorporating chemically linked BTBT cores. Those are the first example of fully crosslinked active layer incorporated in FET thanks to sol–gel process. BTBT $\pi$-conjugated cores are creating conducting pathways for charge carriers inside the hybrid material. The J- to H-aggregation of the compound is controlled by the sol–gel process. The use of a linker, MTES, was the key to improve the covalent aspect and the robustness of the active layer. The HFETs exhibited moderated mobilities due to the intrinsic nature of the hybrid material composed of charge transport organic pathways as well as insulating sublayers made of silicon oxide ($SiO_{1.5}$). However, such devices exhibit an exceptional stability toward thermal annealing in air as well as successive washing in polar and nonpolar solvent even under ultrasonication. Such devices are a first attempt of HFET and show a great potential for a wide range of applications in harsh environments. HFET could be a new family of hybrid devices for the conception of highly robust electronic devices. In a same way, HFET could open the door toward new architectures for sensor applications since the hybrid active layer could be subsequently functionalized by a sensing or a discriminating agent, silylated or not.

Further development on the optimization of the $\pi$-conjugated cores will open the route toward performing hybrid electronics.

CCDC 1528083 contains the supplementary crystallographic data for this paper. These data can be obtained free of charge from The Cambridge Crystallographic Data Centre via www.ccdc.cam.ac.uk/data_request/cif.

## Supporting Information

Supporting Information is available from the Wiley Online Library or from the author.

## Acknowledgements

This study was funded by the "projet blanc ANR-13-BS07-0004 – CrystOS." This work was supported by the Belgian National Fund for Scientific Research (FNRS – Project No. 2.4565.11) and by a concerted research action of theFrench Community of Belgium (ARC Project No. 20061). Y.H.G. was benefited from a mandate of "Francqui Research Professor (2011–2015)." The authors are grateful to Dr. Arie Van der Lee for his support in crystallographic experiments.

## Conflict of Interest

The authors declare no conflict of interest.


© 2017 WILEY-VCH Verlag GmbH & Co. KGaA, Weinheim

## Keywords

field-effect transistors, hybrid materials, nanostructures, organosilica, thin films

Received: May 24, 2017
Published online:

[1] D. Braun, *Mater. Today* **2002**, *5*, 32.
[2] R. H. Friend, R. W. Gymer, A. B. Holmes, J. H. Burroughes, R. N. Marks, C. Taliani, D. D. C. Bradley, D. A. Dos Santos, J.-L. Brédas, M. Löglund, W. R. Salaneck, *Nature* **1999**, *397*, 121.
[3] C. J. Brabec, V. Dyakonov, J. Parisi, N. S. Sariciftci, *Organic Photovoltaics Concepts and Realization*, Springer-Verlag, London **2003**.
[4] C. D. Dimitrakopolous, P. R. L. Malenfant, *Adv. Mater.* **2002**, *14*, 99.
[5] F. J. M. Hoeben, P. Jonkheijm, E. W. Meijer, A. P. H. J. Schenning, *Chem. Rev.* **2005**, *105*, 1491.
[6] A. Mishra, R. K. Behera, P. K. Behera, B. K. Mishra, G. B. Behera, *Chem. Rev.* **2000**, *100*, 1973.
[7] a) E. E. Jelly, *Nature* **1936**, *138*, 1009; b) G. Scheibe, *Angew. Chem.* **1937**, *1*, 212.
[8] L. G. S. Brooker, F. L. White, D. W. Heseltine, G. H. Keyes, S. G. Dent, E. J. VanLare, *J. Photogr. Sci.* **1953**, *1*, 173.
[9] a) E. G. McRae, M. Kasha, *J. Chem. Phys.* **1958**, *28*, 721; b) M. Kasha, H. R. Rawls, M. A. El-Bayoumi, *Pure Appl. Chem.* **1965**, *11*, 371.
[10] A. S. Davydov, *Theory of Molecular Excitons*, Plenum, New York **1971**.
[11] a) O. J. Dautel, G. Wantz, R. Almairac, D. Flot, L. Hirsch, J.-P. Lere-Porte, J. P. Parneix, F. Serein-Spirau, L. Vignau, J. J. E. Moreau, *J. Am. Chem. Soc.* **2006**, *128*, 4892; b) G. Wantz, L. Hirsch, L. Vignau, J.-P. Parneix, O. J. Dautel, F. Serein-Spirau, J.-P. Lere-Porte, J. J. E. Moreau, R. Almairac, *Org. Electron.* **2005**, *7*, 38.
[12] M. Ikai, Y. Maegawa, Y. Goto, T. Taniab, S. Inagaki, *J. Mater. Chem. A* **2014**, *2*, 11857.
[13] T. Cahyadi, J. N. Tey, S. G. Mhaisalkar, F. Boey, V. R. Rao, R. Lal, Z. H. Huang, G. J. Qi, Z.-K. Ng, C. M. Chen, *Appl. Phys. Lett.* **2007**, *90*, 122112.
[14] K. Tetzner, A. K. Schroder, K. Bock, *Ceram. Int.* **2014**, *40*, 15753.
[15] S. Sung, S. Park, W.-J. Lee, J. Son, C.-H. Kim, Y. Kim, D. Young Noh, M.-H. Yoon, *ACS Appl. Mater. Interfaces* **2015**, *7*, 7456.
[16] R.P. Ponce Ortiz, A. Facchetti, J. T. Marks, *Chem. Rev.* **2010**, *110*, 205.
[17] E. C. P. Smits, S. G. J. Mathijssen, P. A. van Hal, S. Setayesh, T. C. T. Geuns, K. A. H. A. Mutsaers, E. Cantatore, H. J. Wondergem, O. Werzer, R. Resel, M. Kemerink, S. Kirchmeyer, A. M. Muzafarov, S. A. Ponomarenko, B. de Boer, P. W. M. Blom, D. M. de Leeuw, *Nature* **2008**, *455*, 956.
[18] A. S. Sizov, E. V. Agina, F. Gholamrezaie, V. V. Bruevich, O. V. Borshchev, D. Yu. Paraschuk, D. M. de Leeuw, S. A. Ponomarenko, *Appl. Phys. Lett.* **2013**, *103*, 043310.
[19] A. V. S. Parry, K. Lu, D. J. Tate, B. Urasinska-Wojcik, D. Caras-Quintero, L. A. Majewski, M. L. Turner, *Adv. Funct. Mater.* **2014**, *24*, 6677.
[20] T. Schmaltz, A. Y. Amin, A. Khassanov, T. Meyer-Friedrichsen, H.-G. Steinrück, A. Magerl, J. J. Segura, K. Voitchovsky, F. Stellacci, M. Halik, *Adv. Mater.* **2013**, *25*, 4511.
[21] A. A. Bessonov, M. N. Kirikova, E. V. Agina, O. V. Borshchev, S. A. Ponomarenko, A. S. Sizov, *WO 2016/064292 A1*, **2016**.
[22] M. F. Calhoun, J. Sanchez, D. Olaya, M. E. Gershenson, V. Podzorov, *Nat. Mater.* **2008**, *7*, 84.
[23] K. Takenami, S. Uemura, M. Funahashi, *RSC Adv.* **2016**, *6*, 5474.
[24] M. Funahashi, *Mater. Chem. Front.* **2017**, *1*, 1137.
[25] O. Knopfmacher, M. L. Hammock, A. L. Appleton, G. Schwartz, J. Mei, T. Lei, P. Jian, Z. Bao, *Nat. Commun.* **2014**, *5*, 2954.
[26] Y. Yuan, G. Giri, A. L. Ayzner, A. P. Zoombelt, S. C. B. Mannsfeld, J. Chen, D. Nordlund, M. F. Toney, J. Huang, Z. Bao, *Nat. Commun.* **2014**, *5*, 1.
[27] J.-M. Cho, T. Higashino, T. Mori, *Appl. Phys. Lett.* **2015**, *106*, 193303.
[28] Y. Tsutsui, G. Schweicher, B. Chattopadhyay, T. Sakurai, J.-B. Arlin, C. Ruzié, A. Aliev, A. Ciesielski, S. Colella, A. R. Kennedy, V. Lemaur, Y. Olivier, R. Hadji, L. Sanguinet, F. Castet, S. Osella, D. Dudenko, D. Beljonne, J. Cornil, P. Samorì, S. Seki, Y. H. Geerts, *Adv. Mater.* **2016**, *28*, 7106.
[29] E. Hideaki, E. Miyazaki, K. Takimiya, M. Ikeda, H. Kuwabara, T. Yui, *J. Am. Chem. Soc.* **2007**, *129*, 15732.
[30] T. Izawa, E. Miyazaki, K. Takimiya, *Adv. Mater.* **2008**, *20*, 3388.
[31] C. Grigoriadis, C. Niebel, C. Ruzié, Y. H. Geerts, G. Floudas, *J. Phys. Chem. B* **2014**, *118*, 1443.
[32] S. Illig, A. S. Eggeman, A. Troisi, L. Jiang, C. Warwick, M. Nikolka, G. Schweicher, S. G. Yeates, Y. H. Geerts, J. E. Anthony, H. Sirringhaus, *Nat. Commun.* **2016**, *7*, 10736.
[33] H. Minemawari, T. Yamada, H. Matsui, J. Tsutsumi, S. Haas, R. Chiba, R. Kumai, T. Hasegawa, *Nature* **2011**, *475*, 364.
[34] H. Iino, T. Usui, J. Hanna, *Nat. Commun.* **2015**, *6*, 6828.
[35] G. Schweicher, V. Lemaur, C. Niebel, C. Ruzié, Y. Diao, O. Goto, W.-Y. Lee, Y. Kim, J.-B. Arlin, J. Karpinska, A. R. Kennedy, S. R. Parkin, Y. Olivier, S. C. B. Mannsfeld, J. Cornil, Y. H. Geerts, Z. Bao, *Adv. Mater.* **2015**, *27*, 3066.
[36] T. Izawa, E. Miyazaki, K. Takimiya, *Adv. Mater.* **2008**, *20*, 3388.
[37] G. H. Roche, Y.-T. Tsai, S. Clevers, D. Thuau, F. Castet, Y. H. Geerts, J. J. E. Moreau, G. Wantz, O. J. Dautel, *J. Mater. Chem. C* **2016**, *4*, 6742.
[38] a) E. G. McRae, M. Kasha, *J. Chem. Phys.* **1958**, *28*, 721; b) A. S. Davydov, M. Kasha, M. Oppenheimer Jr., *J. Chem. Educ.* **1963**, *40*, 142; c) M. Kasha, *Radiat. Res.* **1963**, *20*, 55. d) A. S. Davydov, *Usp. Fiz. Nauk* **1964**, *82*, 393; e) M. Kasha, R. Rawls, M. A. El-Bayoumi, *Pure Appl. Chem.* **1965**, *11*, 371.
[39] Z. Chen, V. Stepanenko, V. Dehm, P. Prins, L. D. A. Siebbeles, J. Seibt, P. Marquetand, V. Engel, F. Würthner, *Chem. - Eur. J.* **2007**, *13*, 436.
[40] Z. Besharat, D. Wakeham, C. M. Johnson, G. S. Luengo, A. Greaves, I. Odnevall Wallinder, M. Göthelid, M. W. Rutland, *J. Colloid Interface Sci.* **2016**, *484*, 279.
[41] D. G. Castner, *Langmuir* **1996**, *12*, 5083.
[42] W. R. Thompson, M. Cai, M. Ho, J. E. Pemberton, *Langmuir* **1997**, *13*, 2291.
[43] H. Tissot, J.-J. Gallet, F. Bournel, A. Naitabdi, D. Pierucci, F. Bondino, E. Magnano, F. Rochet, F. Finocchi, *J. Phys. Chem. C* **2014**, *118*, 1887.
[44] H. Tissot, J.-J. Gallet, F. Bournel, D. Pierucci, M. Silly, F. Sirotti, F. Rochet, *J. Phys. Chem. C* **2014**, *118*, 24397.

 © 2017 WILEY-VCH Verlag GmbH & Co. KGaA, Weinheim